SAND2020-12512J

# Influence of Spatial Dispersion on Spectral Tuning of Phonon-Polaritons

Thomas E. Beechem,[1,2,*] Christopher B. Saltonstall,[1] Tristan Gilbert,[3] Joseph Matson,[3] Fabian Ugwu,[3] Richard Kasica,[4] Francisco J. Bezares,[5] Jason Valentine,[3] and Joshua D. Caldwell[3]

[1]*Sandia National Laboratories, Albuquerque, New Mexico 87123, USA*

[2]*Center for Integrated Nanotechnologies, Sandia National Laboratories, Albuquerque, New Mexico 87185, USA*

[3]*Department of Mechanical Engineering, Vanderbilt University, Nashville, TN, USA*

[4]*National Institute of Standards and Technology, Gaithersburg, Maryland, USA*

[5]*University of Puerto Rico, Cayey, Puerto Rico, USA*

## Abstract

The field of nanophotonics has long sought to identify mechanisms to realize dynamical control of optical modes. In most approaches, the magnitude of tuning is dependent upon the degree to which the optical permittivity is malleable upon some material change, such as carrier concentration. Here, through a multi-wavelength Raman spectroscopic examination of 4H-SiC nanopillars, momentum is identified as an alternative means to enhance spectral tunability of nanophotonic modes owing to the spatial dispersion implicit in the infrared (IR) optical permittivity of polar semiconductors. Experimentally, this is deduced through the observation of a "forbidden" Raman mode at $\approx 780$ and the emergence of the surface-optical phonon at $\approx 950$ cm$^{-1}$ , which evolved with intensities dependent upon the nanopillar diameter and the wavelength of the incident light. The evolution of these modes is accompanied by a red-shift and spectral narrowing of the longitudinal-optical plasmon coupled (LOPC) mode exhibiting a similar wavelength and diameter dependence. Mie resonances, identified using ultraviolet-visible (UV-VIS) spectroscopy and excited by the visible laser excitation of the Raman experiment, acted to vary the momentum sampled during the Raman experiment leading to these spectral dependencies. This was deduced by fitting the Raman response accounting for both the presence of the surface phonon and the overdamped LOPC mode under the Lindhard-Mermin approximation. This fitting not only explains the Raman response, but also clearly exhibits the spatially-disperse permittivity of the SiC, which is shown to have a momentum dependent sensitivity to carrier concentration. Such sensitivity, in turn, highlights the potential of spatial dispersion as a means to accentuate the performance of active IR nanophotonic approaches employing phonon polaritons.


## I. INTRODUCTION

Field-enhancement and sub-diffractional mode confinement drive the pursuit of metasurfaces and nanophotonics for applications ranging from sensing and imaging to home-health diagnostics.[1–3] Multifunctional and dynamically tunable optical devices are also enabled by metasurfaces as the large optical fields they produce amplify the impact of small material property changes.[4–6] Regardless of application, metasurfaces often exploit polaritons,


* tebeech@sandia.gov

quasiparticles emerging from the hybridization of photons with electric-dipoles indigenous to materials (*i.e.*, free-carrier plasmons, polar optical phonons, excitons etc.). [1, 7] These "built-in" dipoles dominate the dielectric function within the spectral region they reside and hence dictate light-matter interactions. Through the formation of such polaritons, light can be confined to dimensions much smaller than the diffraction limit. However, while surface plasmon polaritons (SPPs) have been the most broadly explored polaritons in regards to nanophotonics due to the high modal confinement and fast propagation speeds, they are inherently plagued by resistive losses associated with fast free-carrier scattering.[8] As an alternative, surface-phonon polaritons (SPhPs) are being increasingly pursued despite their slower propagation.[9–11]

Due to the orders of magnitude longer lifetimes associated with optical phonons with respect to free-carrier scattering rates, SPhPs offer dramatically sharper (*i.e.*, narrower linewidth) resonances when realized within nanoantenna geometries. For such systems, the oscillating charge dipole supporting the SPhP proceeds from polar-bonds, which create strong electric fields upon the atomic displacement created by lattice vibrations (*i.e.*, phonons). Surface phonon-polaritons are therefore accessed via polar semiconductors—SiC, [11–13] h-BN,[14–16] GaN,[17, 18] AlN,[19] $SiO_2$,[20, 21] $Al_2O_3$[22] etc.—in a spectral range spanning the transverse- and longitudinal-optical (TO/LO) phonon modes, referred to as the Reststrahlen band. Continued maturation of nascent SPhPs technologies is therefore dependent upon better utilization and potentially the design[23] of the Reststrahlen band.

Reststrahlen materials are intriguing not only for their low loss,[10, 24] but also the potential to engineer and actively tune their optical response. Originating from optical phonons, the Reststrahlen band is thus subservient to changes to the lattice. The optical response is therefore dependent upon strain imparted mechanically[25] or thermally owing to anharmonicity.[26] Similarly, changes in the phonon dispersion realized *via* the growth of atomic scale superlattices using the crystalline hybrid concept have also been used to vary the Reststrahlen response.[23] The modified chemical bonding at the large number of interfaces in such superlattices can also modify the phonon behavior—with interfacial bonding having been demonstrated to induce anomalous spectral shifts in localized SPhP resonances of nanoantennas following atomic-scale deposition of thin oxides.[27] Simply put, due to the phonon-nature of SPhPs, even small modifications to surface vibrations can

strongly impact the IR response of polar materials.

Polar optical phonons are also impacted by the local charge environment. For example, modification of the Reststrahlen response has been demonstrated by altering the free carrier concentration either during synthesis[28, 29] or by photoexcitation.[5, 8] Fundamentally, coupling between the charge, phonons, and photons occurs as each exhibit similar energy and momentum (*i.e.*, phase space). For example, the normal mode of vibration for an optical phonon consists of relative displacement of a cation from an anion leading to an electric field modulated at the frequency of the vibration. This electric field oscillates at frequencies commensurate with that of IR-photons. If each are of similar momentum, they couple and one can induce the excitation of the other. Similarly, charge carriers modify phonons through the Fröhlich interaction and can respond to the incoming electromagnetic field, screen the field, or both. The three-way coupling between charge, photon and phonon is therefore implicit to polar materials.

This strong three-way coupling has long been investigated using Raman spectroscopy through probing of the so-called longitudinal optical phonon plasmon coupled (LOPC) mode.[30, 31] These studies have not only shown the utility of a spectroscopic measurement of carrier concentration and mobility,[32–35] but also provide insights into the optical properties of Reststrahlen materials. For example, Raman studies have highlighted the necessity of employing a momentum (*i.e.*, wavevector) dependent dielectric function to describe polar semiconductors.[32, 36, 37] Within the nanophotonics field, this momentum dependence has most often been ignored, however. From the perspective of SPhPs, momentum dependence of the dielectric function—typically termed spatial dispersion—is of consequence as metasurfaces can impart substantial momentum beyond that of free-space light to an incoming electromagnetic field. Here, in contrast, we show that the spatial dispersion implicit to polar semiconductors is of appreciable consequence in some cases.

Specifically, through a study of the surface-phonon polariton and plasmon-phonon hybrid modes within highly-doped 4H-SiC nanopillars, certain momenta are shown to exhibit much higher changes in permittivity with carrier concentration thereby identifying spatial dispersion as an alternative pathway to dynamically tunable IR nanophotonic devices. Practically, Raman, UV-VIS, and Fourier transform infrared spectrocopies are utilized together to deduce the spatially dispersive permittivity intrinsic to SiC. Subsequently, the implications of this momentum dependence on potential IR dynamic tuning leveraging SPhP in SiC is

explored.

## II. RESULTS AND DISCUSSION

Silicon carbide (SiC) nanopillars with diameters ($\phi$) from nominally 60-200 nm were fabricated into a highly-doped ($3 \times 10^{18}$ cm$^{-3}$) 4H-SiC substrate.[5] The pillars were fabricated using electron beam lithography and reactive ion etching. The nanopillars were etched to a height of ∼600 nm and were spaced from one another by 200 nm. Filling fractions therefore ranged from $\sim$ 4% to 20%. Further details on the fabrication can be found in previous reports.[5, 8, 11, 12]

To examine the coupling of the lattice and charge environments, Raman spectra were acquired at incident wavelengths of 325, 457, 488, and 514 nm focused with a 50X/0.75 NA objective and 0.1-10 mW of incident power using a Renishaw InVia system in the back-scattering geometry. Laser powers were chosen to minimize heating. The spectral resolution is incident wavelength dependent and varied between $\sim 1 - 4$ cm$^{-1}$/px depending on the laser employed. Results were independent of spatial location for a given nanopillar diameter.

The resulting Raman spectra shown in Figure 1 are made up of both features common to the back-scattered response of 4 H−SiC and modes that exhibit dependence to both the laser wavelength employed and the diameter of the nanopillar itself. With respect to the former, the expected $E_2$ (776 cm$^{-1}$ ), E1(TO) (797 cm$^{-1}$ ), and A1(LO) modes. [33, 38, 44] In contrast to previous studies employing undoped SiC nanopillars, the presence of the high free carrier density within this sample results in strong coupling between the LO-optical phonon mode and the free-carrier plasma resulting in the broad LOPC mode observed near 1000 cm$^{-1}$ for the the unpatterned substrate as shown in Figure 1. The $\sim$ 30 cm$^{-1}$ blue-shift of the LOPC mode relative to the Γ−point LO-phonon energy ($\sim$ 964 cm$^{-1}$ ) is in line with expectations for a doping density in the low to mid-$10^{18}$ cm$^{-3}$. [35, 38]

While the smallest nanopillar structures studied ($\phi$=60 nm) exhibited a response nominally unchanged from the underlying 4H-SiC substrate, the Raman spectra display new features as the nanopillar diameter increases. Specifically, a mode appears near 950 cm$^{-1}$ whose intensity is highly dependent upon nanopillar diameter reaching a maximum at $\phi$ =160 nm when analyzed at 514 nm. This same size dependent intensity change is also observed for a second emergent mode near 780 cm$^{-1}$ as is highlighted in Figure 1(c). Accompanying the

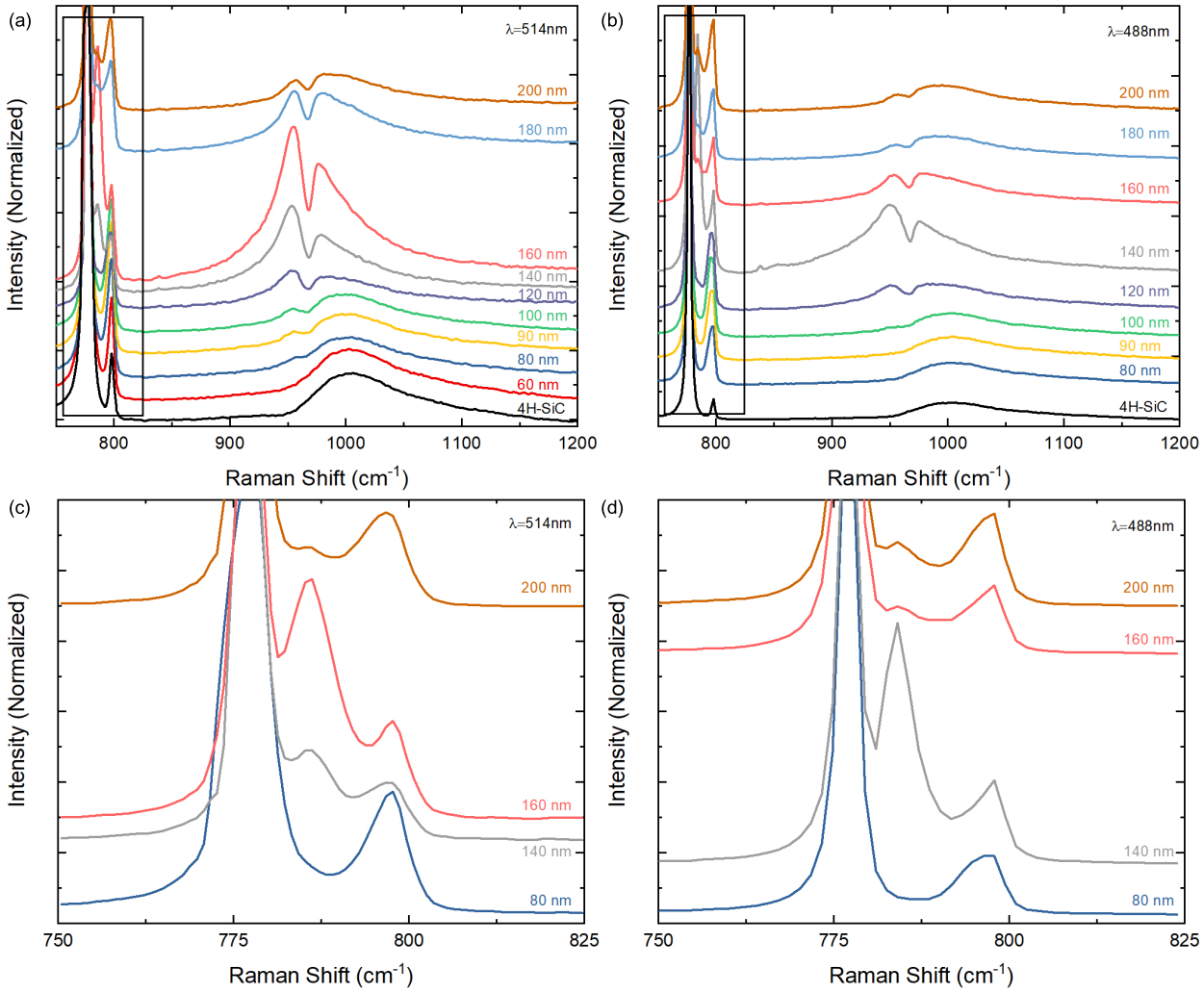


FIG. 1. Raman response of SiC nanopillars of varying diameter acquired with (a,c) 514 and (b,d) 488 nm incident light. Modes emerge near 950 and 780 $cm^{-1}$ whose intensity is dependent upon both the wavelength and nanopillar diameter. To highlight the emergence of the mode near 780 $cm^{-1}$ , (c,d) plot a subset of the data within the range of wavenumbers demarcated by the boxes in (a,b).

appearance of these features, the LOPC changes as well, exhibiting both a size-dependent red-shift and narrowing.

The same qualitative trends are observed when exciting with other wavelengths. However, as is observed upon comparing Figure 1(a,c) acquired using 514 nm light with Figure 1(b,d) collected with 488 nm, the relative intensities of these emergent modes exhibit a nanopillar diameter dependence that is incident wavelength specific. Results obtained with probing

light of 457 and 325 nm exhibit an analogous response (see Supplemental Material Figure S1 [39]) furthering this assertion.

To summarize, the Raman response of the nanopillars presents the expected response of 4H-SiC but with a few notable exceptions. Modes near 776, 796, and 990 $cm^{-1}$ , for example, correspond to the $E_2$, E1(TO) and A1(LO) phonon mode hybridized with the free-carrier plasma, respectively, as predicted from group theory for the $P6_3mc$ symmetry of 4H-SiC.[35, 38] Exceptions occur in the emergent responses at 785 and 960 $cm^{-1}$ , which are not expected in the the z(x-)$\bar{z}$ back-scattering geometry employed here. In addition, the stark changes of intensity that are dependent upon wavelength and diameter cannot be explained with arguments of standard first-order Raman scattering. Thus, these observations suggest that the nanostructuring of the 4H-SiC has changed the nature of the Raman scattering process. In the following, we therefore examine each of these diameter-dependent trends—development of modes at $\sim$780 and 960 $cm^{-1}$ , red-shifting and narrowing of the LOPC, and the wavelength-diameter dependence—using spectral fitting and complementary spectroscopies. In doing so, the spatial dispersion inherent in polar materials is highlighted and its potential for tuning investigated.

The mode near 780 $cm^{-1}$ appears due to selection rule "softening" that occurs with momentum imparted by the dielectric Mie resonance from an individual nanopillar. To support this claim, the nanopillars were examined using UV-VIS spectroscopy implemented using a Horiba iHR 320 spectrometer coupled to a Zeiss AxioObserver inverted microscope, which used a 50X/0.55 NA objective to collect light output from a tungsten halogen lamp. Figure 2(a) plots the resulting scattering from the nanopillars. Resonant features (*i.e.*, largest scattering) are apparent and linearly red-shift with increasing nanopillar diameter as shown in Figure 2(b). To probe the origin of this response, the scattering cross-section of an infinitely long cylinder was calculated utilizing Mie-theory in conjunction with previously published optical properties for 4H-SiC.[40–43] Additionally, finite element analysis (FEA) simulations of a cylinder with $L = 15\phi$ were performed with light incident perpendicular to the long-axis of the SiC cylinder. This simplification was necessary to minimize edge effects in a computationally tractable manner. The wavelength of maximum scattering for a given diameter obtained both from Mie theory and FEA is provided in Figure 2(b) and compared to the resonant features observed in Figure 2(a). The theoretical, computational, and experimental results are quite similar. Mie resonances thus span the entirety of the

visible spectrum for the 60-200 nm SiC nanopillars examined here.

For each Raman excitation wavelength, there is therefore a nanopillar diameter whose Mie resonance aligns with the probing laser. A subset of the Raman response of the nanopillars was therefore acquired when the Mie resonance was stimulated. The impact of the resonance was examined by denoting the laser-wavelength and nanopillar diameter at which the emergent 780 and 950 $cm^{-1}$ modes exhibit their greatest intensity. These combinations correlate closely with both the measured and calculated wavelengths of maximum scattering as is observed in Figure 2(b). We therefore conclude that these modes are born out of the Mie resonance and the impact it has on Raman scattering.

Mechanistically, the Mie resonance impacts the Raman response by concentrating the electric field near the surface and altering the momentum of light participating in the scattering process. The surface concentration, for example, is highlighted by comparing the electric field distributions shown in Figure 2(c) for wavelengths of light "on" and "off" resonance. The electric field near the surface is more than 50x larger than within the center of the cylinder when resonantly excited. Under resonant conditions, the Raman response is therefore harvested primarily from the surface of the nanopillar.

Second, the Mie resonance amplifies the momentum of light relative to the light line and changes its direction. To quantify, Figure 2(d) plots the relative amplitude of participating light-momenta (*i.e.*, wavevectors) deduced by taking a one-dimensional Fourier transform through the center of the transverse electric field distributions in Figure 2(c). When excited by resonant light, wavevectors in excess of $8 \times 10^6$ $cm^{-1}$ participate, which is nearly 100x greater than that of the light-line. Similar momenta do not participate when the nanopillar is probed away from resonance (see inset of Figure 2(d)). The circulating currents stemming from the Mie resonance, meanwhile, change the direction of the wavevector as well.[40] Taken together, we stipulate that these changes in momentum provided by the Mie resonance—accompanied by the field-concentration at the surface—are the genesis for the wavelength and diameter dependent trends observed in the Raman response of Figure 1.

The emergent mode near 780 $cm^{-1}$ , for example, is assigned to the A1(TO) phonon even though it is "forbidden" in the back-scattering arrangement. Here, the mode is observed because the Mie resonance effectively relaxes the Raman selection rules by providing in-plane momentum thereby allowing for observation of the mode.[29] This is analogous to the selection rule softening and emergence of forbidden modes that occur in 4H-SiC when examined

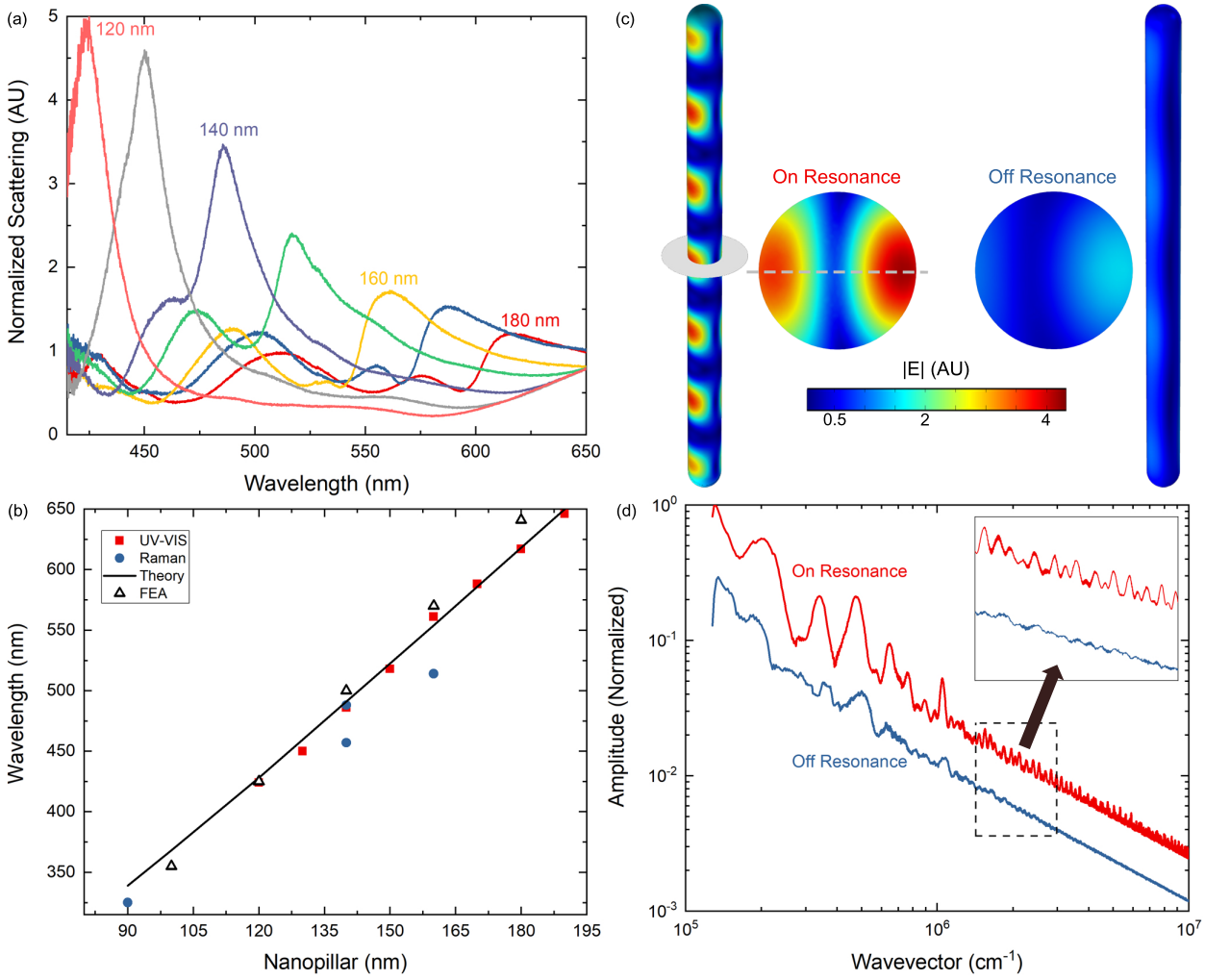


FIG. 2. (a) Normalized light-scattering as a function of wavelength measured *via* UV-VIS spectroscopy. (b) Wavelength of maximum scattering plotted versus nanopillar diameter for measured UV-VIS data, calculated Mie resonance, and deduced from FEA analysis. These are accompanied by the laser-wavelength and nanopillar diameter combinations at which the emergent 780 and 950 $cm^{-1}$ Raman modes exhibit their largest response. (c) Electric field images—norm of the electric field vector—for a $\phi$ =70 nm cylinder both on resonance (500 nm) and off resonance (650 nm). The innermost plots correspond to the field distribution along the transverse plane taken through the cylinder's interior denoted by the gray annulus in the left-most field image. (d) One-dimensional Fourier transform of electric-field profiles taken through the center of the transverse images of (c) as is denoted by dashed-line. At resonance, wavevectors in excess of $10^6$ $cm^{-1}$ participate. Inset: Magnification of region highlighted by dashed box.

with traditional resonant Raman spectroscopy where momentum is supplied by interband transitions.[44] Similarly, disorder also softens selection rules in 4H-SiC as scattering off of defects provides the requisite in-plane momentum.[45] For the nanopillars considered here, the needed momentum is provided by the Mie resonance and thus the intensity of the mode is greatest when excited with resonant light as shown in Figure 1(c,d) and Figure 2(b).

Momentum provided by the Mie resonance is also of consequence in the coupling of the charge and lattice environments, which is the origin of the LOPC mode observed near 1000 $cm^{-1}$ in Figure 1. This is the because the LOPC mode is dependent upon the dielectric function, and the dielectric function of polar materials exhibits a momentum dependence.[36] Changes in the LOPC-mode must therefore be assessed in light of momentum provided by the Mie resonance. For this reason, the Raman response in the region of the LOPC mode (825-1200 $cm^{-1}$ ) was fit to highlight the momentum dependence of the permittivity in 4H-SiC *via* its interaction with the Mie resonance.

From Figure 1(a,c), the LOPC mode red-shifts and narrows with nanopillar diameter. These spectral characteristics are indicative of an overdamped system in which electron scattering occurs at rates higher than the plasma frequency. [30, 32, 34, 46, 47] The 4H-SiC examined here was doped at $3 \times 10^{18}$ $cm^{-3}$ and thus possesses a plasma frequency, $\omega_p = \sqrt{(ne^2)/(\epsilon_o \epsilon_\infty m^*)} = 287$ $cm^{-1}$ , where $n$ is the electron density, $m^* = 0.42$ the electron's effective mass[48] and $\epsilon_\infty = 6.5$ is the high-frequency dielectric constant.[49] All calculations were performed using SI units. The electron scattering rate ($\gamma$) is therefore, $\gamma = e/(\mu m^*) = 889$ $cm^{-1}$ . Since $\gamma > \omega_p$, the system is overdamped as expected from the Raman spectrum. Fitting of this mode must therefore consider its highly-damped behavior.

For overdamped systems, the Raman response of the LOPC is proportional to:[47]

$$I_{LOPC} \propto \sum_i \int_0^{q_{max}} F(q) A_i S_i(q,\omega) \Im\left[-\frac{1}{\epsilon(q,\omega)}\right] dq \tag{1}$$

where $F(q)$ is a momentum dependent weighting function, $S_i(q,\omega)$ a spectral shaping function derived from perturbation theory, $\epsilon(q,\omega)$ the dielectric function, and $\Im\left[-1/\epsilon(q,\omega)\right]$ the energy loss function. The maximum wavevector contributing to the LOPC signal is denoted as $q_{max}$ and is typically taken to be on the order of 5-10 times the Thomas-Fermi wavevector ($q_{TF}$).[47] The sum is over each process influencing the LOPC mode and $A_i$ quantifies relative strength of the $i^{th}$ process. The following provides expressions for each of the remaining terms while also describing the physical processes at play.

The dielectric function is the superposition of the high frequency component ($\epsilon_\infty$) combined with contributions from the phonon ($\epsilon_L$) and charge carrier ($\epsilon_e$) environments expressed mathematically as:

$$\epsilon(q,\omega) = \epsilon_\infty(1 + \epsilon_L(\omega) + \epsilon_e(q,\omega)). \tag{2}$$

First, for the lattice contribution, the influence of transverse and longitudinal optical phonons are accounted for *via* [47]

$$\epsilon_L(\omega) = \frac{\omega_{LO}^2 - \omega_{TO}^2}{\omega_{TO}^2 - \omega^2 - i\omega\Gamma} \tag{3}$$

where $\omega_{LO,TO}$ are the unperturbed phonon energies, which for 4H-SiC are $\omega_{TO} = 796$ and $\omega_{LO} = 964$ cm$^{-1}$ , respectively.[38] Strictly speaking, the phonon energies themselves have a wavevector dependence. However, it is ignored here as the wavevector dependence of the charged environment will dominate owing to the large carrier concentration. $\Gamma$ is the phonon scattering rate taken to be 30 cm$^{-1}$ . This value is consistent with the linear dependence of the damping constant with carrier concentration in 4H-SiC previously reported by Nakashima *et al.* [51, 52]

The Lindhard-Mermin relation is utilized to arrive at the electronic contribution,

$$\epsilon_e(q,\omega) = \frac{(1 + \frac{i\gamma}{\omega})[\chi^o(q,\omega + i\gamma)]}{1 + (i\gamma/\omega)\left(\frac{\chi^o(q,\omega+i\gamma)}{\chi^o(q,0)}\right)} \tag{4}$$

with $\chi^o$ written as,

$$\chi_e^o(q,\omega) = \frac{m^* e^2}{2\pi^2\hbar^2 q^3 \epsilon_o}\int_0^\infty k f(k) \ln\left[\frac{\left(\frac{\hbar^2 q^2}{m^*} + \frac{2\hbar^2 kq}{m^*}\right)^2 - 4\hbar^2\omega^2}{\left(\frac{\hbar^2 q^2}{m^*} - \frac{2\hbar^2 kq}{m^*}\right)^2 - 4\hbar^2\omega^2}\right] dk \tag{5}$$

Within Equation 4, $e$ is the charge of an electron, $\hbar$ is modified Planck's constant, $\epsilon_o$ is the permittivity of free space and $f(k)$ is the Fermi-Dirac distribution at the energy corresponding to the general wavevector, $k$. Noting the wavevector dependence of the dielectric function, the scattering events are weighted to be stronger near the light line using the Yukawa impurity potential such that

$$F(q) = \left(\frac{4\pi}{q^2 + q_{TF}^2}\right)^2 \tag{6}$$

where $q_{TF}$ is the Thomas-Fermi wavevector given by, $q_{TF} = \sqrt{\frac{3m^*}{2E_F}} = 8 \times 10^6$ cm$^{-1}$ . $E_F$ is the Fermi-level calculated using free electron theory.[47] Note that the Thomas-Fermi

wavevector is comparable to the momentum imparted by the Mie resonance ($\approx 10^6$ cm$^{-1}$ , see Figure 2(d)).

Light is an electromagnetic field. In polar materials, the TO and LO phonons themselves induce an electric field as does the charge as it reorients within the crystal. Fields necessarily interact resulting in alterations in the light scattering and hence the measured spectrum. Practically, these effects are quantified using so called shape factors ($S_i(q,\omega)$) that account for: (1) the electric fields induced by the presence of phonons and electrons termed the deformation potential and electro-optic effect (DP+EO) (2) fields caused by charges and phonons interacting with impurities termed the impurity induced Fröhlich interaction (IIF) and (3) that stemming from the density fluctuations of charge at finite temperature termed the charge dissipation fluctuation effect (CDF). Mathematically, these shape factors are given first for the DP-term as,[33, 53, 54]

$$S_{DP+EO}(\omega) = 1 + 2C\omega_{TO}^2 \frac{\omega_p^2\gamma_{PL}(\omega_{TO}^2-\omega^2) - \omega^2\Gamma_{PH}(\omega^2+\gamma_{PL}^2-\omega_p^2)}{\omega_p^2\gamma_{PL}\left[(\omega_{TO}^2-\omega^2)^2+\omega^2\Gamma_{PH}^2\right] + \omega^2\Gamma_{PH}(\omega_{LO}^2-\omega_{TO}^2)(\omega^2+\gamma_{PL}^2)} + \left(\frac{C^2\omega_{TO}^4}{\omega_{LO}^2-\omega_{TO}^2}\right)\frac{\omega_p^2\left[\gamma_{PL}(\omega_{LO}^2-\omega_{TO}^2)+\Gamma_{PH}(\omega_p^2-2\omega^2)\right] + \omega^2\Gamma_{PH}(\omega^2+\gamma_{PL}^2)}{\omega_p^2\gamma_{PL}\left[(\omega_{TO}^2-\omega^2)^2+\omega^2\Gamma_{PH}^2\right] + \omega^2\Gamma_{PH}(\omega_{LO}^2-\omega_{TO}^2)(\omega^2+\gamma_{PL}^2)} \tag{7}$$

where C is the Faust-Henry coefficient ($C_{4H-SiC}$=0.43).[55] The shape factor for the impurity induced Fröhlich interaction, meanwhile, is given by $S_{IIF}(q) = q^2$, while that of the charge dissipation fluctuation is given by,

$$S_{CDF}(\omega) = q^2\left[\frac{\omega_p^2\gamma_{PL}(\omega_{LO}^2-\omega^2)^2 + \omega_p^4\Gamma_{PH}(\omega_{LO}^2-\omega_{TO}^2) + \gamma_{PL}\Gamma_{PH}^2\omega_p^2\omega^2}{\omega_p^2\gamma_{PL}\left[(\omega_{TO}^2-\omega^2)^2+\omega^2\Gamma_{PH}^2\right] + \omega^2\Gamma_{PH}(\omega_{LO}^2-\omega_{TO}^2)(\omega^2+\gamma_{PL}^2)}\right] \tag{8}$$

By employing Equations 1 to 8 together, the LOPC mode shape can be fit to analyze the over-damped system.

There is an additional contribution to the signal as evidenced by the peak-splitting observed in Figure 1(a,b) that originates from the combination of the LOPC mode with that of the SPhP. Surface-phonons can be Raman active but have signals that are typically subsumed by that originating from the bulk of a material. Resonance—and its concomitant momentum—can be leveraged, however, for their observation as has been realized using both near bandgap excitation and diffuse scattering within porous semiconductors.[56–59] Here, the Mie resonance provides the needed surface sensitivity for observation of the SPhPs. The surface phonon polariton [60] was, therefore, fit using an asymmetric lineshape of the

form [61],

$$I_{SPhP} \propto \frac{\left[1 + 2\frac{(\omega-\omega_o)}{\beta\Gamma_F}\right]^2}{1 + \left[2\frac{(\omega-\omega_o)}{\Gamma_F}\right]^2} \tag{9}$$

where $\beta$ is the asymmetry parameter and $\Gamma_F$ is a linewidth value. Note that $\omega_o$ does not equal the SPhP energy, $\omega_{SPhP}$. Rather, $\omega_{SPhP}$ corresponds to the maximum of Equation 9. We will show subsequently the necessity and self-consistency of including the surface-phonon contribution and its fit with an asymmetric lineshape that captures the range of momenta being sampled during the Raman measurement.

In total, the Raman shape from 825-1200 $\text{cm}^{-1}$ was fit by a superposition of the LOPC (Equation 1) and surface-phonon contribution (Equation 9) *via* $I_R = I_{LOPC} + BI_{SPhP} + C$ where B and C are fitted constants that account for the intensity of the SPhP mode and the baseline signal, respectively. Additionally, the maximum wavevector, $q_{max}$, mobility ($\mu$), $\omega_o$, and carrier concentration ($n$) were each treated as fitting parameters. Figure 3 displays the resulting fits for a variety of laser wavelengths and nanopillar diameters both close to, and away from, the Mie resonance. Regardless of condition, the fit is reasonable suggesting that the physical mechanisms included (*i.e.*, LOPC and SPhP) account for the bulk of the behavior. Exact values for the fitted values of $q_{max}$, $\mu$, and $n$ are provided in tables within the Supplemental Material. Weights describing the relative strength of the mechanisms contributing to the spectral response (*i.e.*, $A_i$ and B) were not statistically definitive based on the fit and are not reported for this reason. he following analysis is not impacted by the inability to definitively discriminate between the strength of the individual contributions.

Assessing the fitted parameters provides insight into the physical mechanisms at play. For example, while fitted mobility and carrier concentration remained close to that of the unpatterned film ($\mu \approx 25$ $\text{cm}^2/\text{Vs}$ & $n \approx 10^{18}\text{cm}^{-3}$), the energy ($\omega_{SPhP}$) and intensity (B) of the SPhP, as well as the maximum participating wavevector ($q_{max}$) were highly-dependent upon nanopillar diameter and laser wavelength. Qualitatively, changes in the SPhP intensity are apparent upon examination of Figure 1. Quantitatively, the wavevector dependence is plotted by the markers in Figure 4 where increasing $q_{max}$ nominally correlates with decreases in the SPhP energy. Altogether, these differences imply that the Mie resonance alters the observation of the surface-phonon polariton.

First, the intensity of the SPhP-mode increases near the Mie resonance because the optical near field is concentrated along the surface of the cylinder. Thus, the surface contribution

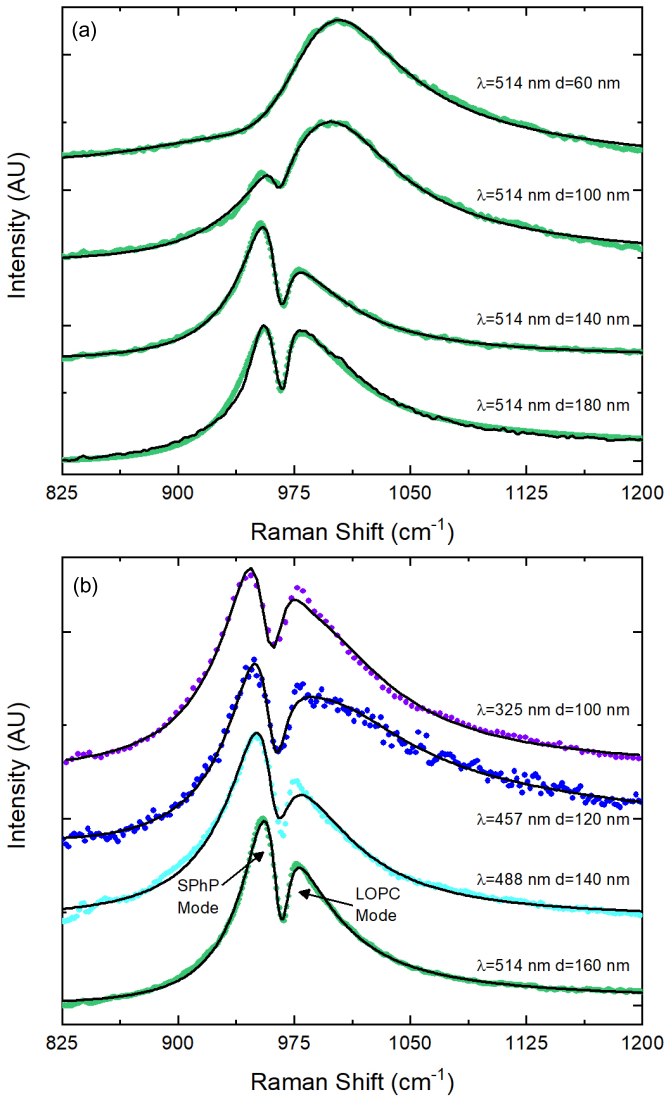


FIG. 3. (a) Normalized fit of the Raman response acquired with 514 nm for a series of different nanopillar diameters both near and far from the Mie resonance. (b) Fitted Raman response for each of the different laser wavelengths for nanopillar diameters near the Mie resonance. All curves are normalized to their maximum value in this range and offset for clarity.

is enhanced upon resonant excitation relative to the total signal.[40] Second, the SPhP energy changes with wavelength and diameter owing to the increased momentum delivered in the near field by the Mie resonance and the wavevector dependent dielectric function of the SiC. This supposition is confirmed by the self-consistency of the SPhP peak positions deduced by multiple methodologies. Specifically, $\omega_{SPhP}$ is of similar value when measured directly from its position in the Raman spectra (*i.e.*, Equation 9) or when deduced from

the permittivity (*i.e.*, $\epsilon(q,\omega)$) obtained from fitting the LOPC mode. With respect to the latter, polar SPhP —Fröhlich modes—are expected for independent cylinders in air when $\epsilon(q,\omega)$ =-1.[58] Using Equation 2 with parameters culled from the LOPC-fit to describe the permittivity, thus provides a straightforward means of calculating the SPhP dispersion, which can then be compared to experiment.

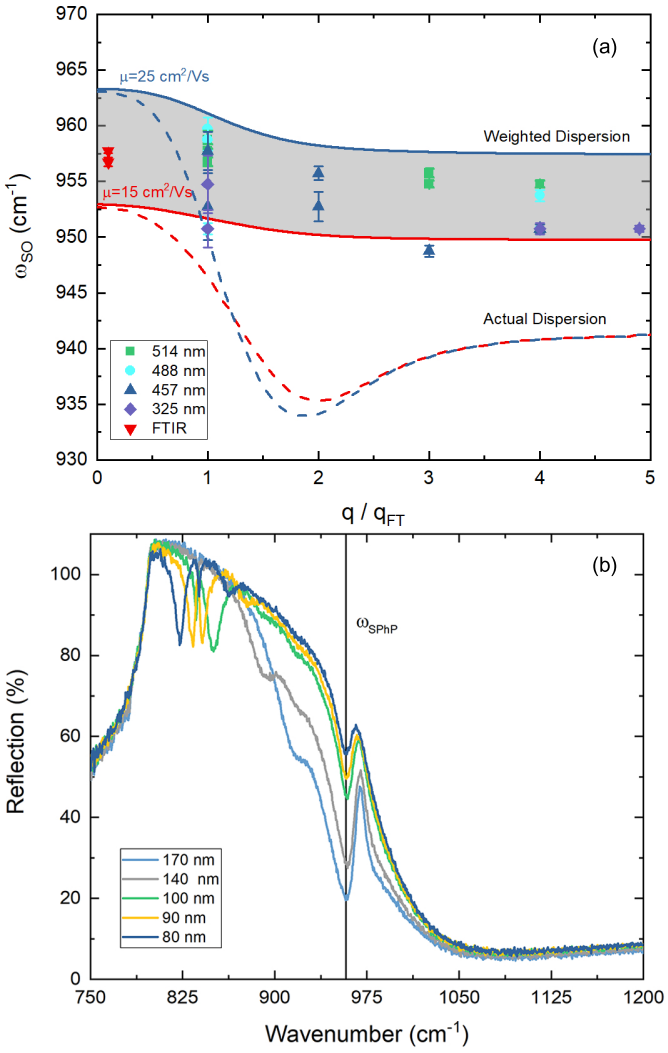


FIG. 4. (a) Surface phonon dispersion (dashed lines) of 4H-SiC at a carrier concentration of $2.5 \times 10^{18}$ cm$^{-3}$ for mobilities of 15 and 25 cm$^2$/Vs. Markers are the fitted locations of the SPhP energy ($\omega_{SPhP}$) plotted against the fitted maximum participating wavevector. Colors denote the laser used in the acquisition of the data. Solid lines are the SPhP dispersion weighted by the Yukawa potential (Equation 6). (b) Measured FTIR spectra of nanopillars in which the surface-phonon energy is invariant with nanopillar diameter.

To that end, the SPhP dispersion is plotted in Figure 4 for nominal mobilities ranging from 15-25 $cm^2/Vs$ and a carrier concentration of $2.5 \times 10^{18}$ $cm^{-3}$. Accompanying these traces, markers plot the fitted peak position of the SPhP mode (Equation 9 and lower energy peak of Figure 3) versus the fitted value of the maximum wavevector participating ($q_{max}$). Comparing the dashed lines of Figure 4(a) with these markers provides insight into the dependence of the measured surface-phonon energies. Theoretically, dispersion links a surface-phonon energy decrease with increasing momentum. Experimentally, positions of $\omega_{SPhP}(q)$ decrease on average with increasing momentum. Together, this suggests that the 5 $cm^{-1}$ decrease in the SPhP energy observed in the Raman measurements is a consequence of sampling across the SPhP dispersion. Sampling across the dispersion is made possible owing to the variable momentum provided by the Mie resonance depending on nanopillar diameter and incident wavelength. In contrast, FTIR measurements sample from only the light line and thus exhibit a near constant surface-phonon energy irrespective of nanopillar diameter as shown in Figure 4(b).

While generally decreasing, the magnitude of reduction in $\omega_{SPhP}(q)$ gathered from the Raman experiment (markers in Figure 4(a)) is much less than that of the SPhP dispersion (dotted lines Figure 4(a)). This discrepancy arises because the Raman experiment does not sample from momentum-space equally, but rather preferentially samples from regions closer to the Γ-point of the Brillouin zone according to the Yukawa potential (see Equation 6). This sampling over a comparatively broad continuum of momentum space leads to the observed Fano-lineshape of the surface phonon and affects its apparent peak energy. To account for the influencing of preferential sampling upon the peak energy, a "Raman-sampled" SPhP dispersion was calculated by taking a weighted average of $\omega_{SPhP}(q)$ using the Yukawa potential— $\bar{\epsilon}(\omega, q) = \int_0^{q_{max}} F(q)\epsilon(\omega, q)dq / \int_0^{q_{max}} F(q)dq$. The resulting "Raman-sampled" dispersion is shown by the solid lines of Figure 4(a), which bound nearly all of the measured results. Taken together, this correlation indicates that the SPhP energy deduced from fits of the LOPC match that measured directly from both Raman and FTIR spectroscopies. The similarity between the three separate methods gives credence to both the model and its fit, thereby allowing for deductions based on the results. Specifically, the results highlight how momentum and spatial dispersion can be leveraged to change light matter interactions in polar materials.

For instance, the spatial dispersion of the permittivity can be leveraged in tandem with

nanostructuring to enhance the dynamic response of tunable infrared devices. Nanostructuring provides access to momenta inversely proportional to the characteristic dimension of the features employed, typically on the order of $10^6$ or even $10^7$ cm$^{-1}$ (see Figure 2(d)). Tip-based methods, for instance, routinely access such momenta as will nanostructures with similar characteristic lengths (*e.g.,* $\approx$ 10-50 nm).[62] At these large momenta, the dielectric function of polar materials can become more sensitive to the carrier concentration. With a larger dependence of the permittivity upon the carrier concentration, greater electrostatic tuning will result. [6, 8]

To demonstrate, consider a hypothetical phonon-polaritonic device built from an electrostatically tuned 4H-SiC grating. Device performance will depend on the ability to excite the SPhP while tuning its energy *via* changes in carrier concentration. When in air, SPhPs are excited only when the real-portion of the 4H-SiC permittivity is <0.[63] Recognizing this constraint, Figure 5 examines the energy at which the real part of the permittivity equals zero (*i.e.*, epsilon near zero (ENZ) energy) as a function of momentum and free carrier concentration calculated using Equations 2 through 7. The degree of ENZ tuning with carrier modulation depends significantly upon momentum reaching a minimum near $10^7$ cm$^{-1}$ and a maximum in the higher mobility case (Figure 5(b,c)) near $6 \times 10^6$ cm$^{-1}$ . Considering that gratings impart a momentum that is proportional to $2\pi/\lambda$, where $\lambda$ is the period, this maximum suggests devices possessing a period of 10 nm period would tune nearly 2x that of one with a 60 nm period if all else is equal.

The tuning dependence based on momentum imparted by the nanostructure is generally applicable and is not specific to the gratings considered here. Similarly, the spatial dispersion of 4H-SiC is an intrinsic material property shared with other polar materials described by similar permittivities (*e.g.,* GaN, AlN, GaAs etc.). Together, the concept thus offers a general opportunity for function in which nanostructuring is designed to not only enhance field concentration within the electrostatically actuated region, but also preferentially sample the momentum space where permittivity is most dynamic. Simply put, momentum provides an additional parameter to enhance performance in dynamically tunable SPhP devices.

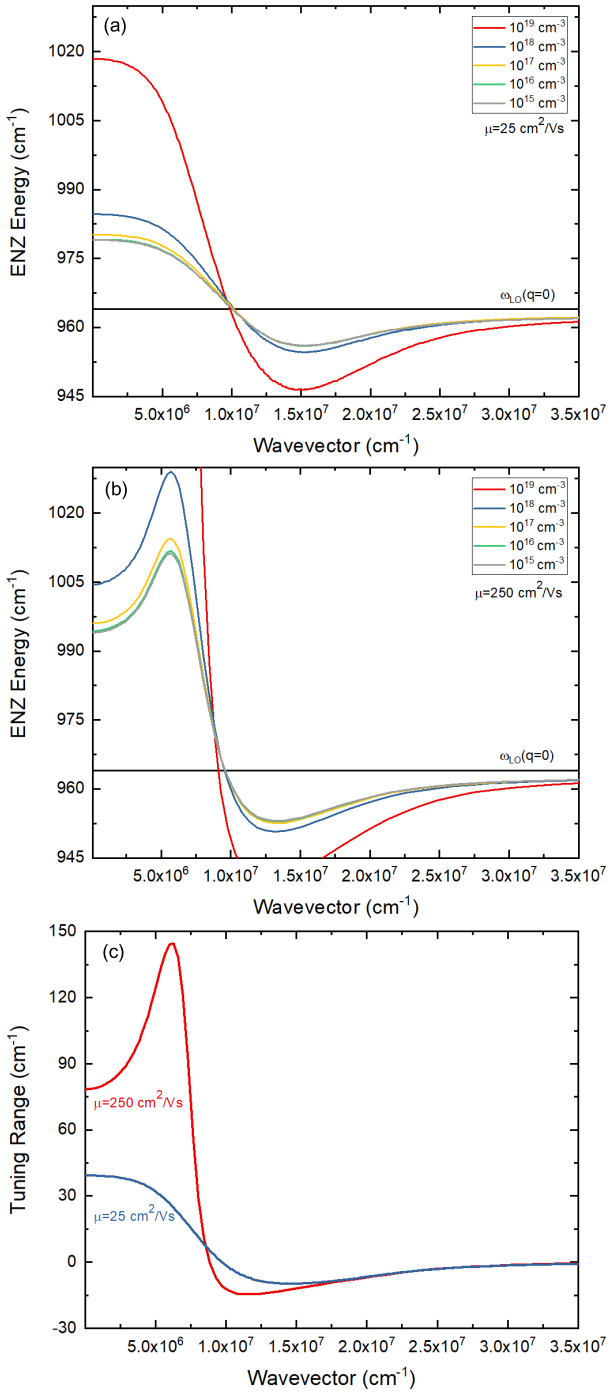


FIG. 5. Energy at which the real part of the permittivity equals zero calculated as a function of momentum at various free carrier concentrations for both (a) low–25 cm$^2$/Vs–and (b) high–250 cm$^2$/Vs–mobilities. (c) Tuning range as quantified by difference in ENZ mode energy when varying carrier concentration from $10^{19}$ to $10^{15}$ cm$^{-3}$. Tuning varies based on momentum.

## III. CONCLUSION

The charge and lattice environments of polar semiconductors create electric fields that interact with each other and external electromagnetic fields. This interaction is momentum dependent and thus so too is the resulting light-matter interaction. Here, using Mie resonances to vary the momentum sampled by Raman spectroscopy measurements of 4H-SiC nanopillars, the inherent spatial dispersion of polar semiconductors resulting from these interactions was highlighted. Spatial dispersion, in turn, can be leveraged in electrostatically tunable polaritonics via nanostructuring that is purposely designed not only for field enhancement but also coupling into the polar materials with a momentum where the permittivity is most dynamic. Momentum is therefore an additional parameter to be leveraged in the design of tunable phonon-polaritonics.

## IV. ACKNOWLEDGEMENTS

Special thanks to Michael Goldflam of Sandia National Laboratories for critical review of this manuscript. This work was performed under the Laboratory Directed Research and Development (LDRD) program at Sandia National Laboratories and undertaken, in part, at the Center for Integrated Nanotechnologies, an Office of Science User Facility operated for the U.S. Department of Energy (DOE) Office of Science. Sandia National Laboratories is a multimission laboratory managed and operated by National Technology & Engineering Solutions of Sandia, LLC, a wholly owned subsidiary of Honeywell International, Inc., for the U.S. DOE's National Nuclear Security Administration under contract DE-NA-0003525. The views expressed in the article do not necessarily represent the views of the U.S. DOE or the United States Government. J.D.C. thanks Prof. Kostya Novoselov for providing access to the Raman instrument where preliminary experiments were performed. J.D.C. acknowledges financial support from the Office of Naval Research and through the Naval Research Laboratory's Long-Term Training (Sabbatical) Program.

[1] T. Low, A. Chaves, J. D. Caldwell, A. Kumar, N. X. Fang, P. Avouris, T. F. Heinz, F. Guinea, L. Martin-Moreno, and F. Koppens, Polaritons in layered two-dimensional materials, Nature

Materials **16**, 182 (2017).

[2] Nano-optics gets practical, Nature Nanotechnology **10**, 11 (2015).

[3] A. Naldoni, V. M. Shalaev, and M. L. Brongersma, Applying plasmonics to a sustainable future, Science **356**, 908 (2017).

[4] Y. Yao, M. A. Kats, P. Genevet, N. Yu, Y. Song, J. Kong, and F. Capasso, Broad electrical tuning of graphene-loaded plasmonic antennas, Nano Letters **13**, 1257 (2013).

[5] B. T. Spann, R. Compton, D. Ratchford, J. P. Long, A. D. Dunkelberger, P. B. Klein, A. J. Giles, J. D. Caldwell, and J. C. Owrutsky, Photoinduced tunability of the reststrahlen band in $4H-$SiC, Physical Review B **93**, 085205 (2016).

[6] M. D. Goldflam, I. Ruiz, S. W. Howell, J. R. Wendt, M. B. Sinclair, D. W. Peters, and T. E. Beechem, Tunable dual-band graphene-based infrared reflectance filter, Optics Express **26**, 8532 (2018).

[7] D. N. Basov, M. M. Fogler, and F. J. García de Abajo, Polaritons in van der waals materials, Science **354**, 10.1126/science.aag1992 (2016).

[8] A. D. Dunkelberger, C. T. Ellis, D. C. Ratchford, A. J. Giles, M. Kim, C. S. Kim, B. T. Spann, I. Vurgaftman, J. G. Tischler, J. P. Long, O. J. Glembocki, J. C. Owrutsky, and J. D. Caldwell, Active tuning of surface phonon polariton resonances via carrier photoinjection, Nature Photonics **12**, 50 (2018).

[9] J. D. Caldwell, L. Lindsay, V. Giannini, I. Vurgaftman, T. L. Reinecke, S. A. Maier, and O. J. Glembocki, Low-loss, infrared and terahertz nanophotonics using surface phonon polaritons, Nanophotonics **4**, 44 (2015).

[10] R. Hillenbrand, T. Taubner, and F. Keilmann, Phonon-enhanced light–matter interaction at the nanometre scale, Nature **418**, 159 (2002).

[11] J. D. Caldwell, O. J. Glembocki, Y. Francescato, N. Sharac, V. Giannini, F. J. Bezares, J. P. Long, J. C. Owrutsky, I. Vurgaftman, J. G. Tischler, V. D. Wheeler, N. D. Bassim, L. M. Shirey, R. Kasica, and S. A. Maier, Low-loss, extreme subdiffraction photon confinement via silicon carbide localized surface phonon polariton resonators, Nano Letters **13**, 3690 (2013).

[12] Y. Chen, Y. Francescato, J. D. Caldwell, V. Giannini, T. W. W. Maß, O. J. Glembocki, F. J. Bezares, T. Taubner, R. Kasica, M. Hong, and S. A. Maier, Spectral tuning of localized surface phonon polariton resonators for low-loss mid-IR applications, ACS Photonics **1**, 718 (2014).

[13] T. Wang, P. Li, D. N. Chigrin, A. J. Giles, F. J. Bezares, O. J. Glembocki, J. D. Caldwell, and T. Taubner, Phonon-polaritonic bowtie nanoantennas: Controlling infrared thermal radiation at the nanoscale, ACS Photonics **4**, 1753 (2017).

[14] J. D. Caldwell, A. V. Kretinin, Y. Chen, V. Giannini, M. M. Fogler, Y. Francescato, C. T. Ellis, J. G. Tischler, C. R. Woods, A. J. Giles, M. Hong, K. Watanabe, T. Taniguchi, S. A. Maier, and K. S. Novoselov, Sub-diffractional volume-confined polaritons in the natural hyperbolic material hexagonal boron nitride, Nature Communications **5**, 5221 (2014).

[15] S. Dai, Z. Fei, Q. Ma, A. S. Rodin, M. Wagner, A. S. McLeod, M. K. Liu, W. Gannett, W. Regan, K. Watanabe, T. Taniguchi, M. Thiemens, G. Dominguez, A. H. C. Neto, A. Zettl, F. Keilmann, P. Jarillo-Herrero, M. M. Fogler, and D. N. Basov, Tunable phonon polaritons in atomically thin van der waals crystals of boron nitride, Science **343**, 1125 (2014).

[16] J. D. Caldwell, I. Aharonovich, G. Cassabois, J. H. Edgar, B. Gil, and D. N. Basov, Photonics with hexagonal boron nitride, Nature Reviews Materials 10.1038/s41578-019-0124-1 (2019).

[17] S. Ng, T. Yoon, Z. Hassan, and H. Abu Hassan, Surface and interface phonon polaritons of wurtzite GaN thin film grown on 6H-SiC substrate, Applied Physics Letters **94**, 241912 (2009).

[18] K. Feng, W. Streyer, S. Islam, J. Verma, D. Jena, D. Wasserman, and A. J. Hoffman, Localized surface phonon polariton resonances in polar gallium nitride, Applied Physics Letters **107**, 081108 (2015).

[19] S. Ng, Z. Hassan, and H. Abu Hassan, Experimental and theoretical studies of surface phonon polariton of AlN thin film, Applied Physics Letters **90**, 081902 (2007).

[20] D. J. Shelton, I. Brener, J. C. Ginn, M. B. Sinclair, D. W. Peters, K. R. Coffey, and G. D. Boreman, Strong coupling between nanoscale metamaterials and phonons, Nano Letters **11**, 2104 (2011).

[21] D.-Z. A. Chen and G. Chen, Measurement of silicon dioxide surface phonon-polariton propagation length by attenuated total reflection, Applied Physics Letters **91**, 121906 (2007).

[22] M. S. Anderson, Enhanced infrared absorption with dielectric nanoparticles, Applied Physics Letters **83**, 2964 (2003).

[23] D. C. Ratchford, C. J. Winta, I. Chatzakis, C. T. Ellis, N. C. Passler, J. Winterstein, P. Dev, I. Razdolski, J. R. Matson, J. R. Nolen, J. G. Tischler, I. Vurgaftman, M. B. Katz, N. Nepal, M. T. Hardy, J. A. Hachtel, J.-C. Idrobo, T. L. Reinecke, A. J. Giles, D. S. Katzer, N. D.

Bassim, R. M. Stroud, M. Wolf, A. Paarmann, and J. D. Caldwell, Controlling the infrared dielectric function through atomic-scale heterostructures, ACS Nano **13**, 6730 (2019).

[24] A. J. Giles, S. Dai, I. Vurgaftman, T. Hoffman, S. Liu, L. Lindsay, C. T. Ellis, N. Assefa, I. Chatzakis, and T. L. Reinecke, Ultralow-loss polaritons in isotopically pure boron nitride, Nature Materials **17**, 134 (2018).

[25] A. M. Gigler, A. J. Huber, M. Bauer, A. Ziegler, R. Hillenbrand, and R. W. Stark, Nanoscale residual stress-field mapping around nanoindents in SiC by IR s-snom and confocal Raman microscopy, Optics Express **17**, 22351 (2009).

[26] A. K. Hafeli, E. Rephaeli, S. Fan, D. G. Cahill, and T. E. Tiwald, Temperature dependence of surface phonon polaritons from a quartz grating, Journal of Applied Physics **110**, 043517 (2011).

[27] J. He and D. R. Clarke, Determination of the piezospectroscopic coefficients for chromium-doped sapphire, Journal of the American Ceramic Society **78**, 1347 (1995).

[28] H. Karakachian and M. Kazan, Dependence of surface plasmon-phonon-polariton in 4H-SiC on free carrier concentration, Journal of Applied Physics **121**, 093103 (2017).

[29] T. E. Tiwald, J. A. Woollam, S. Zollner, J. Christiansen, R. Gregory, T. Wetteroth, S. Wilson, and A. R. Powell, Carrier concentration and lattice absorption in bulk and epitaxial silicon carbide determined using infrared ellipsometry, Physical Review B **60**, 11464 (1999).

[30] T. Kozawa, T. Kachi, H. Kano, Y. Taga, M. Hashimoto, N. Koide, and K. Manabe, Raman scattering from LO phonon-plasmon coupled modes in gallium nitride, Journal of Applied Physics **75**, 1098 (1994).

[31] T. Beechem and S. Graham, Temperature and doping dependence of phonon lifetimes and decay pathways in GaN, Journal of Applied Physics **103**, 093507 (2008).

[32] F. Demangeot, C. Pinquier, J. Frandon, M. Gaio, O. Briot, B. Maleyre, S. Ruffenach, and B. Gil, Raman scattering by the longitudinal optical phonon in InN: Wave-vector nonconserving mechanisms, Physical Review B **71**, 104305 (2005).

[33] M. Chafai, A. Jaouhari, A. Torres, R. Antón, E. Martın, J. Jiménez, and W. Mitchel, Raman scattering from LO phonon-plasmon coupled modes and hall-effect in n-type silicon carbide 4H–SiC, Journal of Applied Physics **90**, 5211 (2001).

[34] G. Irmer, V. V. Toporov, B. H. Bairamov, and J. Monecke, Determination of the charge carrier concentration and mobility in n-GaP by Raman spectroscopy, physica status solidi (b) **119**,

595 (1983).

[35] J. D. Caldwell, O. J. Glembocki, S. M. Prokes, E. R. Glaser, K. D. Hobart, D. M. Hansen, G. Chung, A. V. Bolotnikov, and T. S. Sudarshan, Free carrier distribution profiling of 4H-SiC substrates using a commercial optical scanner, Journal of Applied Physics **101**, 093506 (2007).

[36] G. Abstreiter, M. Cardona, and A. Pinczuk, Light scattering by free carrier excitations in semiconductors, in *Light Scattering in Solids IV* (Springer, 1984) pp. 5–150.

[37] G. Irmer, M. Wenzel, and J. Monecke, Light scattering by a multicomponent plasma coupled with longitudinal-optical phonons: Raman spectra of $p$-type GaAs:Zn, Physical Review B **56**, 9524 (1997).

[38] S. Nakashima and H. Harima, Raman investigation of SiC polytypes, physica status solidi (a) **162**, 39 (1997).

[39] See Supplemental Material at [URL] for Raman results acquired at 457 and 325 nm along with fitted results for mobility, carrier concentration, and the maximum momentum participating in Raman process..

[40] C. F. Bohren and D. R. Huffman, *Absorption and scattering of light by small particles* (John Wiley and Sons, 2008).

[41] J. Schäfer, S.-C. Lee, and A. Kienle, Calculation of the near fields for the scattering of electromagnetic waves by multiple infinite cylinders at perpendicular incidence, Journal of Quantitative Spectroscopy and Radiative Transfer **113**, 2113 (2012).

[42] S. Zollner, J. Chen, E. Duda, T. Wetteroth, S. Wilson, and J. N. Hilfiker, Dielectric functions of bulk 4H and 6H SiC and spectroscopic ellipsometry studies of thin SiC films on Si, Journal of applied physics **85**, 8353 (1999).

[43] S. Wang, M. Zhan, G. Wang, H. Xuan, W. Zhang, C. Liu, C. Xu, Y. Liu, Z. Wei, and X. Chen, 4H-SiC: a new nonlinear material for midinfrared lasers, Laser and Photonics Reviews **7**, 831 (2013).

[44] S.-I. Nakashima, H. Okumura, T. Yamamoto, and R. Shimidzu, Deep-ultraviolet Raman microspectroscopy: Characterization of wide-gap semiconductors, Applied Spectroscopy **58**, 224 (2004).

[45] S. Nakashima, T. Mitani, J. Senzaki, H. Okumura, and T. Yamamoto, Deep ultraviolet Raman scattering characterization of ion-implanted SiC crystals, Journal of Applied Physics **97**, 123507 (2005).

[46] K. Ding, Q. C. Hu, W. W. Lin, J. K. Huang, and F. Huang, Longitudinal optical phonon-plasmon coupled modes of degenerate al-doped zno films, Applied Physics Letters **101**, 031908 (2012).

[47] M. Ramsteiner, O. Brandt, and K. H. Ploog, Overdamped excitations of the free electron gas in GaN layers studied by Raman spectroscopy, Physical Review B **58**, 1118 (1998).

[48] N. Son, W. Chen, O. Kordina, A. Konstantinov, B. Monemar, E. Janzén, D. Hofman, D. Volm, M. Drechsler, and B. Meyer, Electron effective masses in 4H SiC, Applied Physics Letters **66**, 1074 (1995).

[49] L. Patrick and W. Choyke, Static dielectric constant of SiC, Physical Review B **2**, 2255 (1970).

[50] F. Demangeot, J. Frandon, M. A. Renucci, C. Meny, O. Briot, and R. L. Aulombard, Interplay of electrons and phonons in heavily doped GaN epilayers, Journal of Applied Physics **82**, 1305 (1997).

[51] S. Nakashima, T. Kitamura, T. Mitani, H. Okumura, M. Katsuno, and N. Ohtani, Raman scattering study of carrier-transport and phonon properties of $4H-$SiC crystals with graded doping, Physical Review B **76**, 245208 (2007).

[52] S. Nakashima, T. Kitamura, T. Kato, K. Kojima, R. Kosugi, H. Okumura, H. Tsuchida, and M. Ito, Determination of free carrier density in the low doping regime of 4H-SiC by Raman scattering, Applied Physics Letters **93**, 121913 (2008).

[53] S. Guo-Sheng, L. Xing-Fang, W. Hai-Lei, Y. Guo-Guo, D. Lin, Z. Liu, Z. Wan-Shun, W. Lei, Z. Yi-Ping, and L. Xi-Guang, Determination of the transport properties in 4H-SiC wafers by Raman scattering measurement, Chinese Physics B **20**, 033301 (2011).

[54] M. De Biasio, M. Kraft, M. Schultz, B. Goller, D. Sternig, R. Esteve, and M. Roesner, Micro-Raman spectroscopy as a tool for the characterization of silicon carbide in power semiconductor material processing, in *Next-Generation Spectroscopic Technologies X*, Vol. 10210 (International Society for Optics and Photonics) p. 1021014.

[55] A. Zoubir, *Raman imaging: techniques and applications*, Vol. 168 (Springer, 2012).

[56] N. Esser, Analysis of semiconductor surface phonons by Raman spectroscopy, Solid State Communications **69**, 507 (1999).

[57] J. DiGregorio and T. E. Furtak, Raman scattering by surface phonon-polaritons in large SiC microcrystals, Solid State Communications **89**, 163 (1994).

[58] A. Sarua, J. Monecke, G. Irmer, I. M. Tiginyanu, G. Gärtner, and H. L. Hartnagel, Fröhlich modes in porous iii-v semiconductors, Journal of Physics: Condensed Matter **13**, 6687 (2001).

[59] I. Tiginyanu, A. Sarua, G. Irmer, J. Monecke, S. Hubbard, D. Pavlidis, and V. Valiaev, Fröhlich modes in GaN columnar nanostructures, Physical Review B **64**, 233317 (2001).

[60] For large momenta like that provided by the Mie resonances, the surface-phonon polariton approaches the energy of the surface-optical mode. It remains, however, a polariton and is therefore referred to as such throughout this manuscript. The asymptotic approach to the surface optical mode is further leveraged subsequently in deducing the energy of this mode from the dielectric function since it is known that the surface optical mode (or Fröhlich mode) resides at that energy where $\epsilon(\omega, q) = -1$.

[61] A. Ferrari and J. Robertson, Interpretation of Raman spectra of disordered and amorphous carbon, Physical Review B **61**, 14095 (2000).

[62] Z. Fei, G. O. Andreev, W. Bao, L. M. Zhang, A. S. McLeod, C. Wang, M. K. Stewart, Z. Zhao, G. Dominguez, M. Thiemens, M. M. Fogler, M. J. Tauber, A. H. Castro-Neto, C. N. Lau, F. Keilmann, and D. N. Basov, Infrared nanoscopy of dirac plasmons at the graphene–$SiO_2$ interface, Nano Letters **11**, 4701 (2011).

[63] B. Neuner III, D. Korobkin, C. Fietz, D. Carole, G. Ferro, and G. Shvets, Critically coupled surface phonon-polariton excitation in silicon carbide, Optics Letters **34**, 2667 (2009).